

Seismic and aseismic deformation along the East African Rift System from a reanalysis of the GPS velocity field of Africa

Aline Déprez, Cécile Doubre, Frédéric Masson and Patrice Ulrich

IPGS, Université de Strasbourg/EOST, CNRS 5 rue Descartes, 67084 Strasbourg Cedex, France. E-mail: a.deprez@unistra.fr

Accepted 2013 March 1. Received 2013 February 27; in original form 2012 September 12

SUMMARY

The improvement of the geodetic coverage within the African Plate over the last decade together with an extended GPS position time-series allows improved accuracy in determining the velocity field than prior geodetic studies. Using this new velocity field of the whole African continent, the best model proposed here remains consistent with previous studies including the existence of two small plates along the East African Rift System (EARS, Victoria and Rovuma). We focus specifically on the velocities along this plate boundary by estimating both the geodetic and the seismic moment rate. Whereas we use a scalar form of the Kostrov relation to calculate the geodetic moment rate, the seismic moment rate is obtained by integrating the cumulative truncated Gutenberg–Richter earthquake distribution of local events in the 39-yr-long worldwide catalogue, using a maximum likelihood method. This statistical method allows us to take into account the probable incompleteness of the existing catalogue and to assume the seismic moment rate calculated from this short catalogue to be representative of the long-term seismic deformation. The comparison of geodetic and seismic energy release sheds light on the variations of mechanical behaviour related to intracontinental extension along the EARS. The southward increase, observed along the rift, of the proportion of geodetic moment seismically accommodated suggests a significant control of the thermal structure associated with different states of rifting evolution.

Key words: Plate motions; Continental tectonics: extensional; Africa.

1 INTRODUCTION

The East African Rift System (EARS) is the largest seismically and volcanically active rift above sea level. This mainly intracontinental divergent boundary runs over 3000 km from Mozambique to the triple junction of Arabia–Nubia–Somalia plates in Afar. The seismic activity in East Africa prominently underlines this north–south system, drawing seismic belts that delimit largely aseismic blocks (Fig. 1). The extensive deformation shows different stages, from intracontinental extension, continental break-up, to eventually incipient oceanic spreading in northern Afar (Hayward & Ebinger 1996; Ebinger & Casey 2001; Chorowicz 2005; Delvaux & Barth 2010). The geological models, which provide an average motion over several million years, offer a first and global estimate of the kinematics of the EARS (Jestin *et al.* 1994) with an opening rate ranging from 1 to 5 mm yr⁻¹ on its northern part (north of 22°S). Southward, the kinematics of such models is more ambiguous, and some authors have considered this part as a diffuse extension zone up to 2000-km wide (Grimison & Chen 1988). On a smaller scale, the spatial organization of the extensive deformation is complex, with different orders of segmentation characterizing the EARS system. The first-order segmentation is related to the five individual ~1000-km-long branches: the Main Ethiopian Rift (MER), the

Western and the Eastern (Kenya Rift) branches surrounding the Tanzanian craton the Malawi Rift and the Davie Ridge (Fig. 2). The second-order segmentation delimits 50–100-km-long segments (Chorowicz 2005), concentrating the tectonic or/and the volcanic activity (Ebinger 1989a,b; Ebinger *et al.* 1993; Hayward & Ebinger 1996; Delvaux & Khan (1998); Kurz *et al.* 2007). The complexity of the boundary therefore makes both the short-term and the long-term kinematics of the EARS difficult to understand. The recent geodetic data offer a good opportunity to make both the geometry and the extent of this boundary more precise, together with its extension rates. As suggested by previous studies using either GPS and slip vector data (Calais *et al.* 2006) or only geodetic data (Stamps *et al.* 2008), geodetic models require two smaller plates in addition to the large Nubia and Somalia plates, to account for the observed velocity field: the Victoria Plate, also called Ukerewe Nyanza (Hartnady 2002), which encompasses the Tanzanian craton and further south the Rovuma Plate. This latter plate is supposed to be bounded by the Malawi Rift at the West and by the Davie Ridge on its eastern side but the geometry of their northern and southern borders remains partly unknown. However, the geodetic models for East Africa suffer from both the lack of a homogeneous network with a dense distribution of the GPS stations and the short time span of the time-series of the most of the geodetic data.

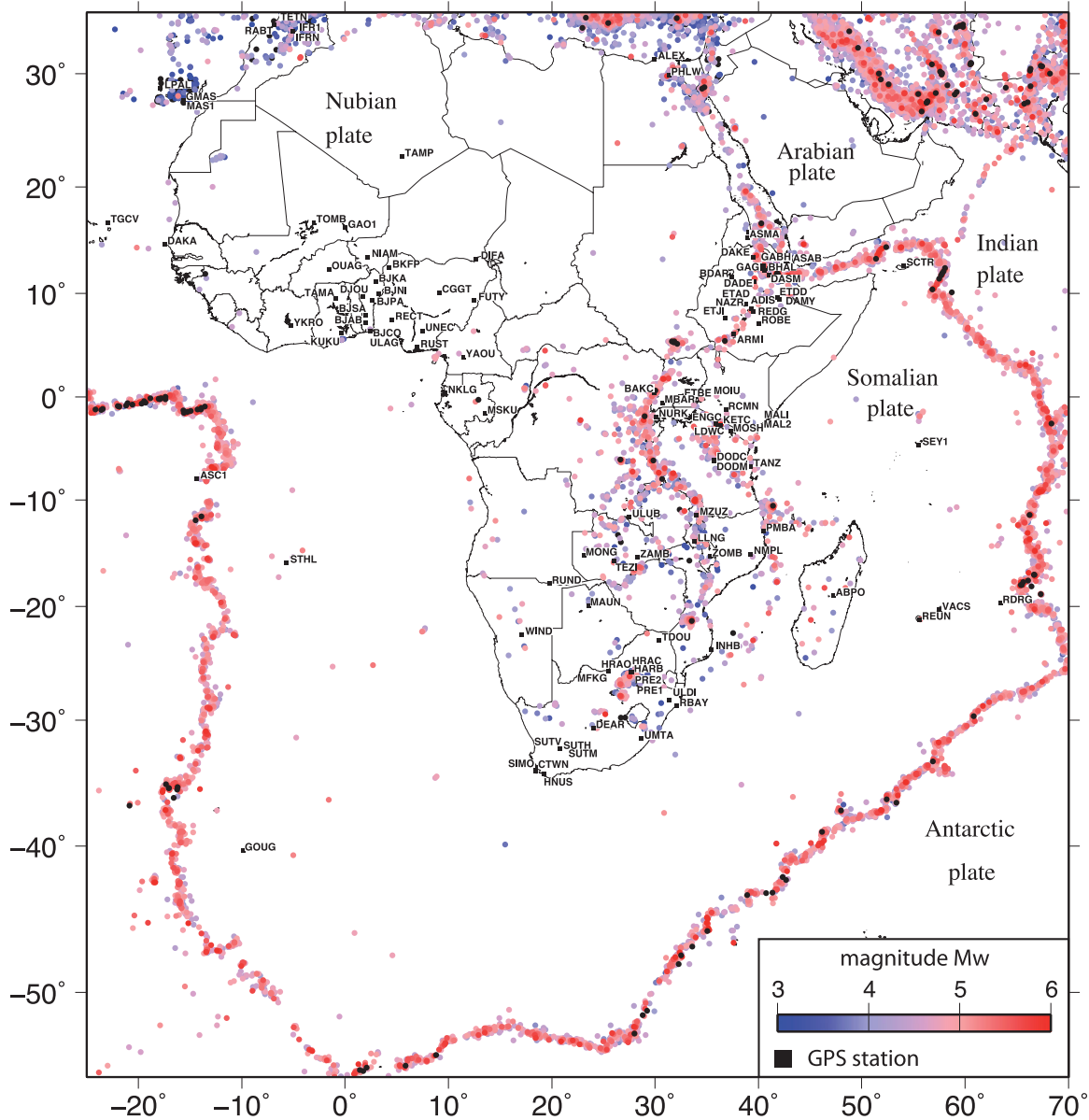


Figure 1. Map of the seismicity and the continuous GPS stations used in this study. The colour scale depicts the magnitude of the seismicity. Most of the seismicity in Africa is located along the EARS. Events with a magnitude greater than 6 (black dots) are scarce.

In this study, after re-evaluating this four-plate model in light of longer time-series and more GPS stations since the last decade, we focus on the seismic/aseismic behaviour of the first-order segments of the EARS by comparing seismic and geodetic moment rates. We then analyse the variations of the ratio of seismic and geodetic extension rates taking into account the knowledge of the evolution of the continental breakup stages along the whole EARS, in particular the thermal state of the lithosphere (Bilham *et al.* 1999; Keir *et al.* 2006; Yang & Chen 2010) and therefore the influence of variable asthenospheric processes along the branches of the EARS (George *et al.* 1998; Ebinger & Casey 2001; Nyblade 2011).

2 DATA AND PROCESSING

Over the last decade a large number of new continuous GPS stations have been installed in Africa, significantly increasing the available data set. Combined with an increase of the time span of the for-

mer GPS observations, we aim to obtain a geodetic velocity field of Africa and improve the solution compared to previous studies (Calais *et al.* 2006; Stamps *et al.* 2008). To do so, we collect all possible data from the African continuous GPS stations from 1999 to 2011.

We include ~ 90 continuous GPS stations in the processing (Fig. 1). We select 11 reliable sites around the world for the stabilization of the network with respect to the ITRF2008 (GLSV GRAZ IISC JOZE KIT3 MAS1 ONSA POL2 RABT VILL ZIMM). We process our data set using the GAMIT/GLOBK software version 10.4 (King & Bock 2010), leading to daily position time-series and absolute velocity with respect to ITRF2008 for each station (Table 1). In order to estimate accurate data uncertainties, we model the noise of the time-series by the sum of white noise and flicker noise, as done by previous studies (Zhang *et al.* 1997; Mao *et al.* 1999). The CATS software (William 2003, 2008) is used to compute the amplitude of the components of both noises. As expected,

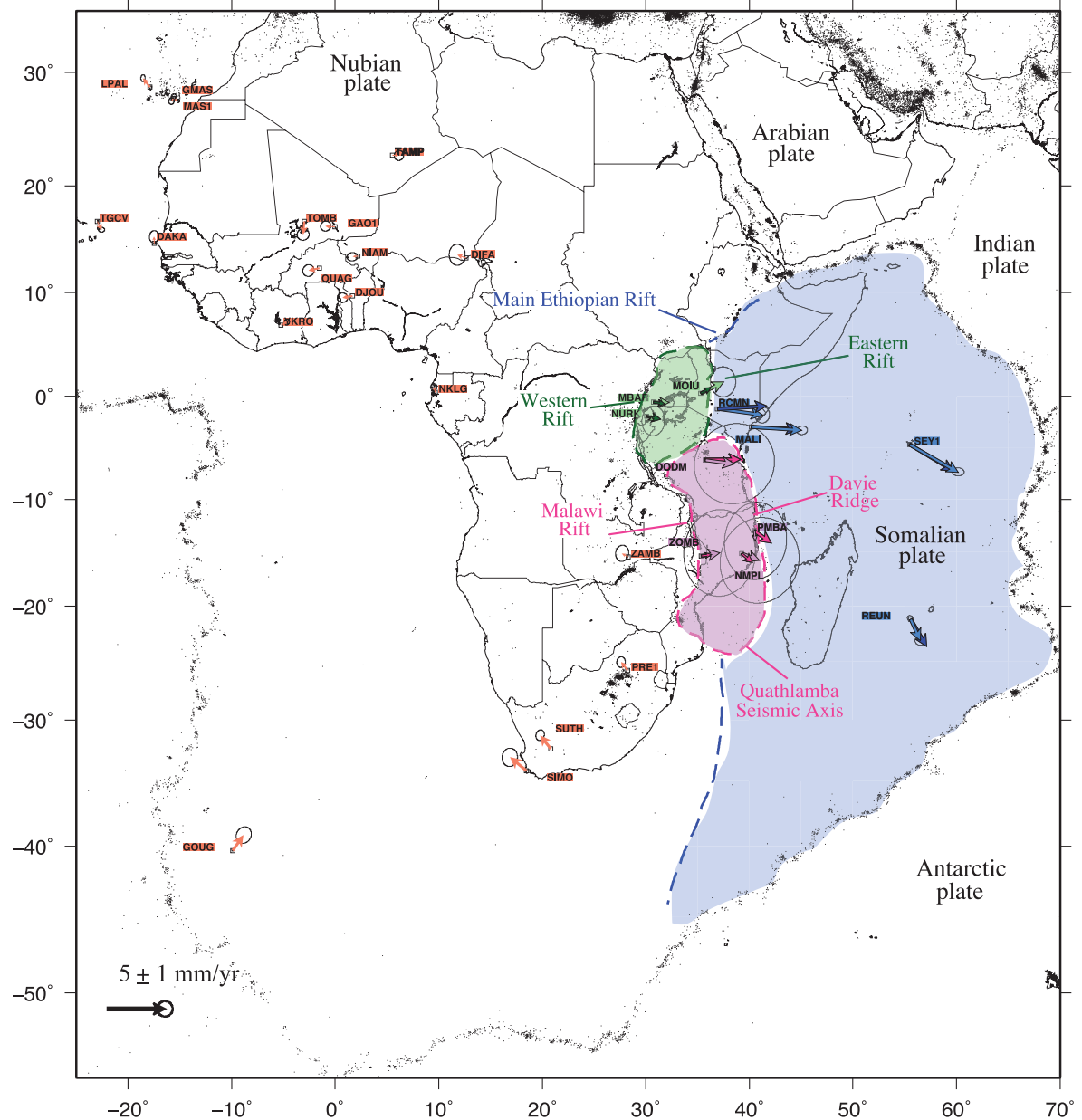


Figure 2. Velocities w.r.t. Nubia. On the Nubian Plate, only the sites used for the pole determination are drawn. On the other plates, 2 arrows are drawn for each site. The light colour arrow shows the observed velocity w.r.t. Nubia. The dark colour arrows shows the theoretical movement of the site w.r.t. Nubia deduced from the Euler poles determined by the inversion of the geodetic velocity field for each plate.

the velocity error decreases when the time span of the observations increases. For the oldest stations, corresponding to 12 yr of data acquisition, the errors on both the north and east components are $\sim 0.3 \text{ mm yr}^{-1}$.

3 EULER POLES DETERMINATION

By inverting the geodetic velocity field previously calculated, we estimate the Euler pole coordinates and the angular velocity of each plate independently with respect to the ITRF2008 (Figs 2 and 3). We split our data set into four subsets of continuous GPS stations following the four-plate model of Calais *et al.* (2006) and Stamps *et al.* (2008): ~ 60 sites on the Nubia Plate, nine on the Somalia Plate, eight on the Victoria Plate, seven on the Rovuma Plate. In addition of being uneven, the data subsets present large differences,

since most of the sites on the two small plates are located along their boundaries. Therefore, due to a significant dissimilarity of the available data set between the Nubia Plate and the other plates, we follow a specific approach for the determination of the pole for the Nubia Plate.

3.1 Nubia

To avoid any miscalculation of the rotation vector, which characterizes the motion in a rigid plate model on a sphere, a careful selection of the sites included in the inversion is needed. We start using a subset of spatially well-distributed sites according to the three following conditions:

- (1) The horizontal component velocity uncertainties are smaller than 0.7 mm yr^{-1} .

Table 1. GPS site velocities with respect to ITRF-2008 and in the Nubia fixed reference frame.

Site	Lon	Lat	V_e ITRF08	V_n ITRF08	V_e fixed Nubia	V_n fixed Nubia	σ_e	σ_n	Corr.
DIFA	12.60631	13.31236	19.26	17.18	-0.75	0.27	1.04	1.37	-0.015
DJOU	1.66164	9.69206	18.81	16.58	-0.86	-0.16	0.67	0.62	0.027
GAO1	359.99399	16.25212	17.91	16.71	-0.83	0.05	0.66	0.65	0.053
GMAS	344.36573	27.76478	14.45	15.03	-0.16	-0.21	0.35	0.44	0.082
GOUG	350.11929	-40.34883	20.22	17.27	0.94	1.37	0.99	1.08	0.144
LPAL	342.10617	28.76387	13.44	15.69	-0.61	0.75	0.28	0.44	0.047
MAS1	344.36673	27.76374	15.04	15.02	0.42	-0.22	0.17	0.22	0.280
NIAM	2.18319	13.47926	18.80	16.71	-0.48	-0.05	0.69	0.54	0.045
NKLG	9.67213	0.35391	20.24	17.39	-0.14	0.47	0.41	0.43	0.050
OUAG	358.48750	12.35639	18.22	16.36	-0.96	-0.21	0.73	0.76	0.050
PRE1	28.22404	-25.74634	15.51	16.81	-0.57	0.72	0.55	0.69	0.052
SIMO	18.43957	-34.18794	14.06	17.93	-1.42	1.19	1.00	1.19	0.039
SUTH	20.81046	-32.38021	14.61	17.80	-0.92	1.17	0.55	0.69	0.139
TAMP	5.52965	22.79265	18.83	16.85	0.56	-0.02	0.61	0.65	0.040
TGCV	337.01724	16.75477	17.23	13.44	0.37	-0.74	0.40	0.31	0.070
TOMB	357.00255	16.73065	18.32	15.35	-0.10	-1.13	0.78	0.74	0.039
YKRO	354.75991	6.87056	20.22	16.60	0.52	0.28	0.34	0.39	0.083
ZAMB	28.31101	-15.42554	17.70	16.37	-0.54	0.29	0.85	1.06	0.075
MALI	40.19440	-2.99591	24.32	14.35	4.40	-0.29	0.70	0.55	0.069
RCMN	36.89348	-1.22083	24.13	14.58	3.91	-0.53	0.95	1.08	0.011
REUN	55.57172	-21.20823	15.48	10.02	0.84	-1.85	0.68	0.60	-0.042
SEY1	55.47941	-4.67372	23.55	9.49	4.21	-2.40	0.77	0.52	-0.022
MBAR	30.73788	-0.60147	21.69	15.80	1.37	-0.037	0.59	0.67	0.011
MOIU	35.29001	0.28832	22.37	16.30	1.95	0.99	1.64	1.96	-0.011
NURK	30.08968	-1.94455	20.75	15.50	0.57	-0.40	1.48	1.94	0.036
DODM	35.74817	-6.18646	22.00	14.92	2.52	-0.33	5.22	5.22	0.055
NMPL	39.25794	-15.12283	19.08	14.18	1.55	-0.60	5.14	5.56	0.056
PMBA	40.48383	-12.96446	18.04	13.70	0.09	-0.90	4.05	5.05	0.049
ZOMB	35.32513	-15.37584	19.36	15.59	1.61	0.28	4.65	5.64	0.024

(2) The time span of observations is longer than 8 yr.

(3) The site must be far from any kind of known local deformation.

Therefore, sites close to or within the seismically active areas and/or plate boundaries are excluded. This is the case in Northern Africa (Moroccan sites TETN, IFR1, IFRN and RABT), in East Africa close to the Ethiopian rift (DAKE, BDAR, BHAL, DAMY, ROBE, ARMI, NAZR, ETJI, ADIS and ETAD) and along the Red Sea side (SHEB and ASMA).

By estimating the Nubian Euler pole with five reliable sites, (NKLG, GMAS, NIAM, MAS1, PRE1, choice of these sites based on the time-series), we obtain a weighted rms (WRMS) on the residual horizontal velocities of 0.3 mm yr^{-1} . Then we consider every possible six-site subset independently, including the previous sites and one additional station. We estimate the consistency of additional data with the rigid rotation previously defined by using the F -ratio statistic (Nocquet *et al.* 2002, 2006). The final data set used as input in the inversion consists of 19 stations indicated on the map of the Fig. 2. We obtain a solution for the Nubia-ITRF2008 angular velocity (Table 2) with a WRMS on the horizontal velocities of 0.5 mm yr^{-1} and a reduced χ^2 of 1.42. The residual horizontal velocities are lower than 1.8 mm yr^{-1} for the 19 sites.

It is important to note that the horizontal velocities at 13 sites considered unreliable due to their short time-span observations (less than 3 yr—BJKA, UNEC, MAUA, BJPA, CTWN, ULUB, SUTV, BJCO, MZUZ, PHLW, SUTM, PRE2 and TAMA) are nevertheless consistent with the estimated pole, since their residual velocities with respect to the stable Nubian Plate model are lower than 1.7 mm yr^{-1} .

3.2 Somalia

Due to the small number of sites on the Somalia Plate (9), we evaluate the pole using all the sites assumed to belong to the plate. In order to check the consistency of each site with the data set, we look at the effect of removing this site on the WRMS value after inversion. Using this approach, we select only four stations (REUN, RCMN, SEY1 and MALI) to constrain the pole with a WRMS of 0.4 mm yr^{-1} . Three stations (MAL2, SCTR and VACS) are not included in the inversion but are consistent with the calculated pole, since their residual velocity in the Somalia reference frame is lower than 1.5 mm yr^{-1} . On the contrary, the site on Madagascar Island (ABPO) and the site along the Indian ridge (RDRG) present an unexpected residual velocity of 1.8 and 1.7 mm yr^{-1} , respectively.

3.3 Victoria

After following the same approach for the Victoria Plate, we finally determine its angular velocity using GPS velocity at only three sites (MOIU, MBAR and NURK), which is lower than the total amount of stations located within the plate (8). The resulting WRMS is 0.3 mm yr^{-1} and the maximum residual velocity is 0.9 mm yr^{-1} .

3.4 Rovuma

The WRMS resulting from the inversion of data from four sites assumed to belong to the Rovuma Plate (ZOMB, DODM, NMPL and PMBA) is 0.7 mm yr^{-1} . The residual velocities are lower than 0.7 mm yr^{-1} , excepted for PMBA where the residual velocity is 1.4 mm yr^{-1} .

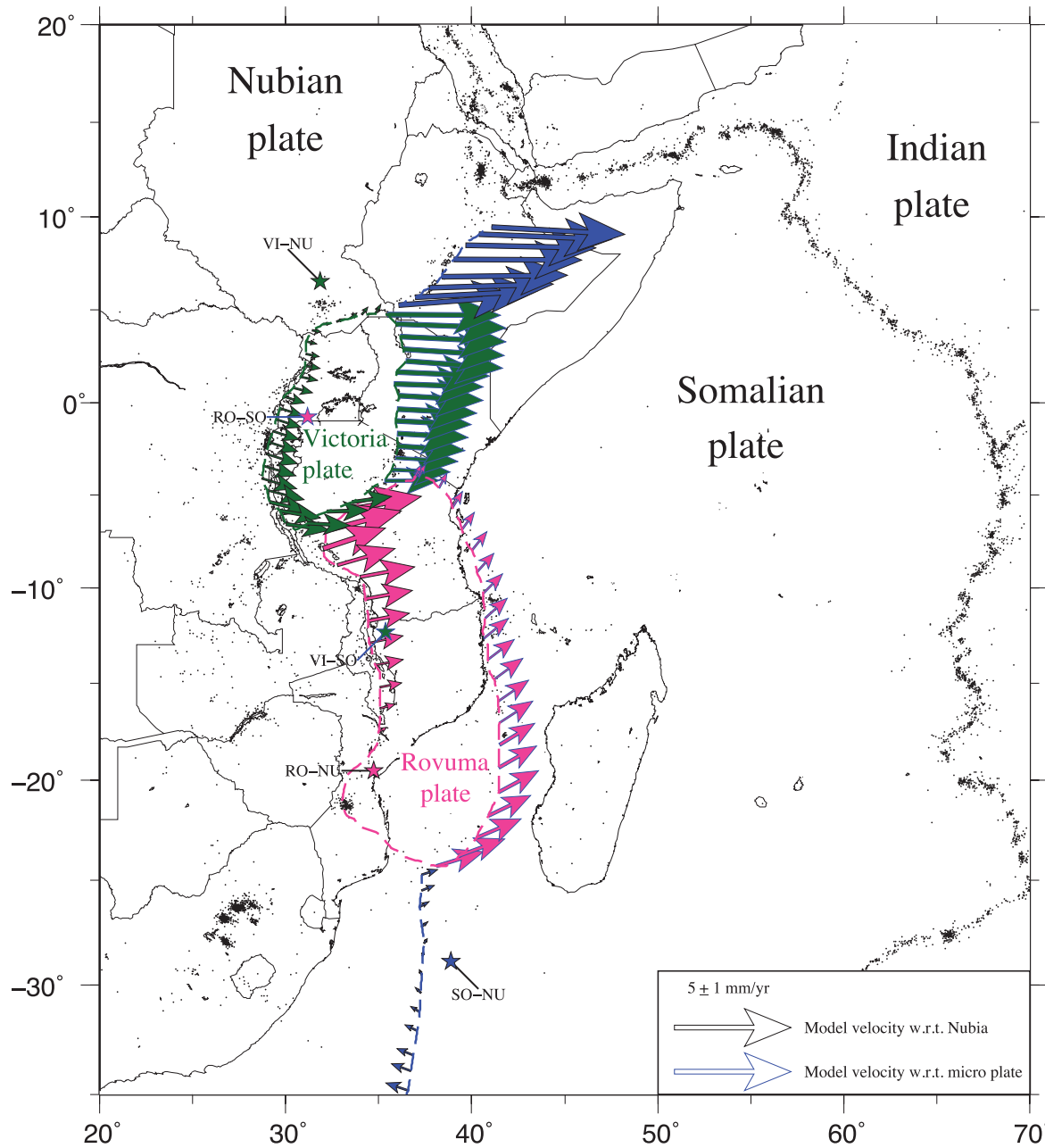


Figure 3. Relative velocities along the EARS. According to Calais *et al.* (2006), we use a four-plate model and define the plate borders by following the seismicity. The velocities are deduced from the Euler poles determined by an inversion of the geodetic velocity field for each plate.

Table 2. Euler pole coordinates with respect to the ITRF-2008. Between brackets: Nubia pole coordinates obtained by Altamimi *et al.* (2012).

Plate	Lat	Lon	Ang	σ_{lat}	σ_{lon}	σ_{ang}
Nubia	50.30465 (49.4493)	-79.88782 (-81.0435)	0.23844 (.2671)	0.0041 (0.2448)	0.0165 (0.7058)	0.0015 (0.0012)
Somalia	-48.50120	81.31849	-0.29851	0.0288	0.0428	0.0106
Victoria	53.79063	-62.49425	0.24154	0.0432	1.4459	0.0109
Rovuma	-44.27138	72.48177	-0.32118			

Despite the high uncertainties, the trend of the velocities changes along the EARS on either sides of the E–W-trending Kenya–Tanzania border located at latitude $\sim 5^\circ\text{S}$. Further north, the most probable E–W velocity component calculated at each site (MOIU, MBAR and NURK) is slightly positive or almost null, whereas the same velocity component of the southernmost sites (DODM,

ZOMB, PMBA and NMPL) is negative or almost null. This observation confirms the need for an E–W Plate boundary south of the Tanzanian craton (Calais *et al.* 2006). In our model, this border follows the Usangu rift (Le Gall *et al.* 2004).

Our four-plate model is roughly similar to the previous models proposed by Calais *et al.* (2006) and Stamps *et al.* (2008). Such a

similarity, with a database enhanced by a great number of sites and an accurate uncertainty estimate of the velocities, leads us to be confident about the geodetic model and to enlarge the scope of our work. In the following, we adopt an approach combining geodetic and seismic data. This kind of comparison reveals that geodetic measurements give a fundamental contribution to characterize the main features of the strain field.

4 GEODETIC AND SEISMIC MOMENT RATES

The comparison of the seismic and geodetic deformation is important for understanding both the tectonic deformation and earthquake hazard assessment (Papazachos & Kiratzi 1992; Ward 1998; Shentu *et al.* 1998; Kreemer *et al.* 2000; Jenny *et al.* 2004; Masson *et al.* 2005; Panha *et al.* 2006; D'Agostino *et al.* 2009). However, such comparison suffers from its dependency on the existing seismic catalogue, and great caution must be taken on the estimate of the seismic moment rates. There is a great likelihood that the amplitude of the seismic deformation rate in a given region based on instrumental seismicity would either be significantly lower or larger than the long-term one, due to the short duration (a few decades) of the seismic catalogue (Kreemer *et al.* 2002; Masson *et al.* 2005). Nevertheless, in this study we show that the systematic greatly lower seismic moment rates compared to the geodetic ones along some of the ~ 1000 -km-long segments of the EARS cannot be reasonably only assigned to the incompleteness of the short duration catalogue, following the approach developed in Mazzotti *et al.* (2011) and detailed in the following Section 4.2.

In order to study the geodetic strain and its seismic accommodation in East Africa, we look closer at the five main branches of the EARS. The first branch encompasses the Main Ethiopian Rift corresponding to the northern Nubia–Somalia boundary and the four following segments are the EARS Western Branch, the Malawi Rift, the EARS Eastern Branch and the Davie Ridge, which figure the Nubia–Victoria, the Nubia–Rovuma, the Victoria–Somalia and the Rovuma–Somalia boundaries, respectively.

4.1 Geodetic moment rate

We compute the spatial evolution of the geodetic strain along the segments of the main branches, by calculating the velocities along the plate boundaries using the rotation poles of the Somalia, Victoria and Rovuma plates deduced from the previously calculated geodetic model (Fig. 3).

To do so, we use a sliding rectangular window with a 100-km-wide step (Fig. 5). Two sides of the window with length (l) are parallel to the velocity vector calculated at the centre of the box, the two other sides are 300-km long (L). Assuming that both magnitude and direction of the velocity are constant over time within the window, the geodetic strain rate ($\dot{\epsilon}$) is defined by the ratio between the velocity and the box width (l).

$$\dot{\epsilon} = \frac{v}{l}. \quad (1)$$

Then, we estimate the geodetic moment rate using the definition of the strain tensor rate given by Kostrov (1974).

$$2\mu AH_S \dot{\epsilon} = \dot{M}_{\text{geodetic}} \quad (2)$$

using μ the shear modulus taken to 3×10^{10} N m $^{-2}$, $A = l \times L$ the box surface area and H_S the seismogenic thickness. In order to take into account the effect of the presence of the Afar hotspot on the

elastic thickness of the lithosphere, we choose $H_S = 25$ km along the Main Ethiopian Rift and $H_S = 30$ km from southern Ethiopia to the southernmost part of the rift (Ebinger *et al.* 1989). Note that the geodetic moment rate is independent of the box width.

4.2 Seismic moment rate

We estimate the seismic moment rate by using the scalar moment of the seismic events recorded within the zone. The scalar approach has been chosen because of the weakness of the CMT catalogues for the EARS due to both the low magnitude of most of the earthquakes occurring in this region (Bendick *et al.* 2006) and the sparse seismic network. First, we combine the NEIC and ISC earthquake catalogues. In order to unify these catalogues, we consider that the m_b magnitude given by the ISC and NEIC agencies are the same, according to many previous studies (e.g., Rezapour 2005; Scordilis 2006). Then we determine a linear relation (Eq. 3) between body wave magnitudes (m_b) and moment magnitudes (M_w), using a set of earthquakes, for which both M_w and m_b magnitudes are determined.

$$M_w = 0.8363m_b + 1.013. \quad (3)$$

We note that this relation is consistent with the results of Scordilis (2006), who established in particular an empirical relation to convert m_b into M_w using a very large sample of data over the world.

The range of magnitude of the earthquakes used in this study is relatively narrow. We only consider the events with a magnitude M_w higher than or equal to $m_0 = 4.7$, considered as the completeness magnitude by plotting the log cumulative number of earthquake against magnitude. The highest magnitude recorded along the EARS is 7.0, corresponding to the earthquake in Mozambique on 2006 February 22.

Within each box defined along the EARS, we estimate the seismic moment rate using the following relation (eq. 4, Hyndman & Weichert 1983), which is obtained by integrating the Gutenberg–Richter log-linear distribution up to a maximum magnitude M_X .

$$\dot{M}_{\text{seismic}} = \varphi \frac{b}{(c-b)} 10^{[(c-b)M_X + a + d]}, \quad (4)$$

where φ is a correction factor due to the asymmetric relation between magnitude and moment, Hyndman & Weichert (1983) advised for $\varphi = 1.27$, reflecting a standard error of 0.2 on magnitudes. c and d are the parameters used for the conversion from magnitude m into seismic moment M_0 [$\log_{10}(M_0) = cm + d$]. In our case, taking advantage of the previous determination of the magnitude M_w for all earthquakes, we use the relation defined by Kanamori (1977), which yield $(c, d) = (1.5, 9.1)$. M_X is the assumed maximum magnitude. We use one maximum magnitude value for every box along the same segment, which is taken equal to the highest magnitude recorded in the catalogue along the segment. This led us to use the following values: $M_X = 5.7$ along the Main Ethiopian Rift, $M_X = 5.9$ along the Eastern Branch of the Tanzanian Craton, $M_X = 6.8$ along the Western Branch of the Tanzanian Craton, $M_X = 6.5$ along the Malawi Rift, $M_X = 6.4$ along the Davie Ridge. a and b are the intercept and the slope of the Gutenberg–Richter recurrence relation respectively (eq. 5).

$$\log N = a - bM. \quad (5)$$

We use the maximum likelihood method, first defined by Weichert (1980), to calculate these parameters: the maximum likelihood estimate of the seismicity level, a , is the total number of

Table 3. Moment rates along the MER and earthquake catalogue statistics. $\dot{M}_{\text{geodetic}}$: moment rate based on the GPS data, calculated using the Kostrov relation. b : best-fitting slope of the Gutenberg–Richter recurrence relation (eq. 5). N : number of earthquakes used for the magnitude–frequency fit. \dot{M}_{seismic} : moment rate based on the earthquake catalogue, calculated using a statistical method with different maximum magnitude (M_X) and a summation method. Min and Max values presented for \dot{M}_{seismic} correspond to the bounds of the 67 per cent confidence interval.

	$\dot{M}_{\text{geodetic}}$ (10^{17} Nm yr $^{-1}$)	b (+/–)	N	\dot{M}_{seismic} (10^{17} Nm yr $^{-1}$)			\dot{M}_{seismic} (10^{17} Nm yr $^{-1}$)	\dot{M}_{seismic} (10^{17} Nm yr $^{-1}$)
				$M_X = 5.7$				
				Median	Min	Max		
Box1	25.77	1.30 (0.19)	22	1.00	0.17	9.57	1.58	0.41
Box2	25.19	1.40 (0.24)	15	1.22	<0.06	12.07	1.53	0.50
Box3	24.76	0.93 (0.10)	12	0.25	0.04	0.85	0.94	0.18
Box4	24.22	0.92 (0.15)	16	0.33	0.04	1.77	1.27	0.30
Box5	23.86	0.91 (0.12)	18	0.44	0.07	1.77	1.73	0.20
Box6	23.59	1.01 (0.14)	16	0.53	0.07	2.59	1.63	0.21
Box7	23.35	1.03 (0.17)	16	0.48	0.04	3.02	1.40	0.27
Box8	25.46	1.21 (0.22)	16	0.69	0.04	7.61	1.33	0.30

Table 4. Reconciliation between seismic and geodetic moment rates, along the MER. $\dot{M}_{\text{geodetic}}/\dot{M}_{\text{seismic}}$: ratio between geodetic and seismic moment rates. $\dot{M}_{\text{geodetic}} - \dot{M}_{\text{seismic}}$: difference between geodetic and seismic moment rates. T7 (respectively T6) difference between geodetic and seismic moment rates expressed as equivalent return period of $M_W = 7$ (respectively $M_W = 6$) earthquakes (Mazzotti *et al.* 2011).

$\dot{M}_{\text{geodetic}}/\dot{M}_{\text{seismic}}$			$\dot{M}_{\text{geodetic}} - \dot{M}_{\text{seismic}}$ (10^{17} Nm yr $^{-1}$)			T7			T6		
Mean	Min	Max	Mean	Min	Max	Mean	Min	Max	Mean	Min	Max
26	3	155	24.77	16.19	25.60	16	15	25	0.5	0.5	0.8
21	2	>390	23.97	13.12	25.19	17	16	30	0.5	0.5	1
99	29	576	24.51	23.90	24.71	16	17	16	0.5	0.5	0.5
74	14	689	24.42	23.00	24.72	16	16	17	0.5	0.5	0.5
55	14	358	23.78	22.45	24.15	17	16	18	0.5	0.5	0.6
45	9	368	23.33	21.27	23.80	17	17	19	0.5	0.5	0.6
50	8	544	23.12	20.57	23.55	17	17	19	0.5	0.5	0.6
37	3	725	24.78	17.85	25.43	16	16	22	0.5	0.5	0.7

Table 5. Moment rates along the Eastern branch of the Tanzanian Craton and earthquake catalogue statistics (same fields as Table 3).

	$\dot{M}_{\text{geodetic}}$ (10^{17} Nm yr $^{-1}$)	b (+/–)	N	\dot{M}_{seismic} (10^{17} Nm yr $^{-1}$)			\dot{M}_{seismic} (10^{17} Nm yr $^{-1}$)	\dot{M}_{seismic} (10^{17} Nm yr $^{-1}$)
				$M_X = 5.9$				
				Median	Min	Max		
Box1	16.53	1.27 (0.14)	39	1.82	0.28	7.63	3.09	0.72
Box2	15.49	1.14 (0.11)	47	1.78	0.35	6.12	4.05	1.15
Box3	14.49	1.19 (0.10)	65	2.57	0.60	7.69	5.28	1.49
Box4	13.51	1.17 (0.09)	73	2.84	0.74	7.76	6.07	1.58
Box5	12.60	1.25 (0.10)	66	2.86	0.68	8.31	5.15	1.19

earthquakes above the magnitude of completeness (m_0 , defined above) and an estimate of b is given by a formula equivalent to

$$b = \frac{\log 10}{(\bar{m} - m_0)}, \quad (6)$$

where \bar{m} is the average magnitude of the sample.

5 DISCUSSION

5.1 GPS and earthquake catalogue moment rates comparison

In order to estimate the seismic moment rate over a period, one could simply normalize by the period duration the cumulative estimated moments for the recorded events (method that we call ‘summation method’ in the following). However the use of this method suffers from the possible lack of both large earthquakes, with high recurrence rate compare to the catalogue duration and the unde-

tected, small magnitude events, which leads to large statistical errors (Hyndman & Weichert 1983). The statistical method adopted in this study is therefore more rigorous, since it takes into account the incompleteness of the catalogue using the magnitude distribution of the events through the estimate of the b value. We obtained seismic moment rate values, which differ from these obtained by using the ‘summation method’: the ratio between the two seismic moment rate estimates ranges from 0.06 to 1.5 (Tables 3–12).

Nevertheless the ratio between seismic and geodetic moment rates follows a similar evolution along the main branches of the EARS whatever the method used to estimate the seismic moment rate: a low seismic moment rate for the most northeastern branches (MER and Eastern Rift, see Sections 5.2 and 5.3) and a good agreement of the seismic and geodetic moment rates for the other segments mainly located in the southern part of the EARS (Western Rift, Malawi Rift and Davie Ridge, see Sections 5.4–5.6).

As described in the Section 4.2, the seismic moment rate calculation depends on the choice of the maximum magnitude (M_X)

Table 6. Reconciliation between seismic and geodetic moment rates, along the Eastern branch of the Tanzanian Craton (same fields as Fig. 4).

$\dot{M}_{\text{geodetic}}/\dot{M}_{\text{seismic}}$			$\dot{M}_{\text{geodetic}} - \dot{M}_{\text{seismic}} (10^{17} \text{ Nm yr}^{-1})$			T7			T6		
Mean	Min	Max	Mean	Min	Max	Mean	Min	Max	Mean	Min	Max
9	3	60	14.71	8.90	16.25	27	24	45	0.9	0.8	1.4
9	2	44	13.71	9.37	15.14	29	26	42	0.9	0.8	1.3
6	2	24	11.92	6.80	13.89	33	29	59	1.1	0.9	1.9
5	2	18	10.67	5.75	12.77	37	31	69	1.2	1	2.2
4	2	19	9.74	4.29	11.92	41	33	93	1.3	1.1	2.9

Table 7. Seismic moment rates along the Western branch of the Tanzanian Craton and earthquake catalogue statistics (same fields as Tables 3 and 4).

	$b (+/-)$	N	$\dot{M}_{\text{seismic}} (10^{17} \text{ Nm yr}^{-1})$ $M_x = 6.8$			$\dot{M}_{\text{seismic}} (10^{17} \text{ Nm yr}^{-1})$ $M_x = 7.8$	$\dot{M}_{\text{seismic}} (10^{17} \text{ Nm yr}^{-1})$ 'summation'
			Median	Min	Max		
Box1	1.23 (0.18)	30	2.32	0.20	19.62	4.32	0.73
Box2	1.23 (0.14)	53	4.10	0.59	21.59	7.60	1.93
Box3	1.42 (0.16)	48	5.73	<0.86	26.16	6.90	1.53
Box4	1.29 (0.12)	69	4.85	0.90	19.55	7.79	1.79
Box5	1.29 (0.12)	69	4.85	0.90	19.55	7.79	1.79
Box6	1.16 (0.09)	84	6.18	1.71	17.78	13.53	1.94
Box7	1.15 (0.08)	87	6.57	1.98	17.51	14.71	1.99
Box8	1.23 (0.08)	68	5.19	1.58	13.27	9.71	0.93
Box9	1.04 (0.11)	54	5.22	1.08	19.44	15.18	6.42
Box10	1.00 (0.10)	71	7.28	1.57	25.54	22.80	9.08
Box11	0.97 (0.08)	100	10.88	3.07	30.08	36.72	12.57

Table 8. Geodetic moment rate along the Western branch of the Tanzanian Craton and ratio between geodetic and seismic moment rates (same fields as Tables 3 and 4).

	$\dot{M}_{\text{geodetic}} (10^{17} \text{ Nm yr}^{-1})$	$\dot{M}_{\text{geodetic}}/\dot{M}_{\text{seismic}}$		
		Median	Min	Max
Box1	3.53	1.5	0.2	17
Box2	4.12	1	0.2	7
Box3	4.74	0.8	0.2	>5
Box4	5.44	1.1	0.3	6
Box5	6.23	1.3	0.3	7
Box6	6.95	1.1	0.4	4
Box7	7.61	1.2	0.4	4
Box8	8.26	1.6	0.6	5
Box9	8.93	1.7	0.5	8
Box10	9.49	1.3	0.4	6
Box11	10.16	0.9	0.3	3

value, that we take here equal to the maximum magnitude observed in the earthquake catalogue within each branches. This choice can be discussed and in order to enhance the weight of our conclusions we re-evaluate the seismic moment rate by using a magnitude

maximum with an increment of 1 compared to the first calculation. The increase of the seismic moment rate induced by this change is not associated with major consequence on our seismic/geodetic comparison, since it allows reducing the gap between seismic and geodetic rates along the 2 southernmost segments. But the discrepancy between the two kinds of measurement stays very large along the MER. At the Southern end of the Eastern Rift, the discrepancy is less prominent but stays consistent with the observations of Calais *et al.* (2008) with more than the half of the deformation aseismically accommodated (Tables 3–12).

In order to justify our conclusion on the aseismic behaviour along the northeastern branches, we quantify the difference between the GPS and the seismic catalogue-based moment rates in terms of the return period of $M_w = 6$ earthquakes (Mazzotti *et al.* 2011). This magnitude is consistent with field observations, such as fault length and slip length on faults, along these branches (Asfaw 1998; Williams 2003), which are admittedly magmatic examples of segment related to continental breakup (Ebinger & Casey 2001). Moreover $M_w = 6$ is greatly higher than the catalogue magnitude completeness ($M_w = 4.7$).

Table 9. Seismic moment rates along the Malawi rift and earthquake catalogue statistics (same fields as Table 3).

	$b (+/-)$	N	$\dot{M}_{\text{seismic}} (10^{17} \text{ Nm yr}^{-1})$ $M_x = 6.5$			$\dot{M}_{\text{seismic}} (10^{17} \text{ Nm yr}^{-1})$ $M_x = 7.5$	$\dot{M}_{\text{seismic}} (10^{17} \text{ Nm yr}^{-1})$ 'summation'
			Median	Min	Max		
Box1	0.94 (0.12)	40	3.15	0.52	14.29	11.51	3.64
Box2	1.09 (0.18)	22	1.48	0.12	13.27	3.83	0.50
Box3	1.13 (0.14)	43	2.80	0.39	14.91	6.58	0.88
Box4	1.17 (0.15)	43	2.76	0.34	16.25	5.94	0.78
Box5	1.11 (0.16)	31	2.04	0.21	14.21	4.94	0.65
Box6	0.90 (0.19)	16	1.32	0.09	13.83	5.23	1.90
Box7	0.84 (0.20)	13	1.17	0.07	13.89	5.35	1.78
Box8	1.45 (0.36)	6	1.00	<0.01	36.42	1.12	0.07

Table 10. Geodetic moment rate along the Malawi rift and ratio between geodetic and seismic moment rates (same fields as Fig. 3).

	$\dot{M}_{\text{geodetic}}$ (10^{17} Nm yr $^{-1}$)	$\dot{M}_{\text{geodetic}}/\dot{M}_{\text{seismic}}$		
		Median	Min	Max
Box1	15.41	5	1	30
Box2	13.93	9	1	120
Box3	12.95	5	0.9	34
Box4	11.50	4	0.7	34
Box5	10.05	5	0.7	48
Box6	8.28	6	0.6	94
Box7	6.56	6	0.5	96
Box8	4.85	5	0.1	>300

From the north to the south along the EARS, we observe a general decrease of the geodetic moment rate, which roughly corresponds to an increase of the seismic moment rate. This is clearly observed (in blue, Fig. 4) along the eastern side of the EARS (i.e. from the Main Ethiopian Rift to the Davie Ridge through the Eastern branch of the Tanzanian Craton, Fig. 4), where the gap between seismic and geodetic moment rates at the North is largely reduced at the South. Along the western side (in red, Fig. 4), even if the agreement between seismic and geodetic data seems to be better on the northern part (western branch of the Tanzanian Craton) than on the southern one (Malawi Rift), the potential large earthquakes expected in the Lake Malawi vicinity (Jackson & Blenkinsop 1997) would greatly impact the shape of the seismic moment rate curve.

5.2 The Main Ethiopian Rift and the northern part of the Eastern Rift

Along the northernmost segment of the EARS, the Main Ethiopian Rift splits Africa into Nubia and Somalia with a velocity of about 5 mm yr $^{-1}$ (Fig. 6). This opening rate is the highest value for the whole EARS, which is explained by both the high distance of the Nubia-Somalia rotation pole and the uniqueness of the spreading axis at this latitude of the EARS. Geological kinematic models (Joffe & Garfunkel 1987; Jestin *et al.* 1994) and previous GPS studies (Fernandes *et al.* 2004; Bendick *et al.* 2006; Calais *et al.* 2006; Kogan *et al.* 2012) on this EARS section testify to intense ongoing deformation. At the surface, the MER is characterized by large active volcanoes and neogene volcanism (Chorowicz 2005) and large scarps of normal faults. Further south, the EARS is divided into two branches on both sides of the 600-km-wide Tanzanian craton. The Eastern branch is thought to be the direct continuation of the MER (Ebinger *et al.* 2000). We estimate the seismic moment rate at the northern tip of this branch but the very low number of earthquakes prevents us to calculate it for the branch centre.

Table 11. Seismic moment rates along the Davie Ridge and earthquake catalogue statistics (same fields as Fig. 3).

	b (+/−)	N	\dot{M}_{seismic} (10^{17} Nm yr $^{-1}$)			\dot{M}_{seismic} (10^{17} Nm yr $^{-1}$)	\dot{M}_{seismic} (10^{17} Nm yr $^{-1}$)
			$M_x = 6.4$				
			Median	Min	Max		
Box1	1.06 (0.21)	11	0.68	0.04	8.24	1.90	0.25
Box2	1.45 (0.29)	6	0.99	<0.03	16.71	1.10	0.06
Box3	1.40 (0.17)	32	3.16	<0.41	15.97	3.93	0.42
Box4	1.08 (0.12)	50	3.06	0.53	12.98	8.05	1.82
Box5	1.09 (0.12)	54	3.29	0.62	12.90	8.46	1.81
Box6	0.98 (0.12)	25	1.66	0.28	7.02	5.54	0.78
Box7	1.09 (0.18)	7	0.43	0.03	3.62	1.11	0.13
Box8	1.41 (0.37)	12	1.22	<0.02	59.37	1.51	0.19

Table 12. Geodetic moment rate along the Davie Ridge and ratio between geodetic and seismic moment rates (same fields as Fig. 3).

	$\dot{M}_{\text{geodetic}}$ (10^{17} Nm yr $^{-1}$)	$\dot{M}_{\text{geodetic}}/\dot{M}_{\text{seismic}}$		
		Median	Min	Max
Box1	4.91	7	0.6	135
Box2	5.52	6	0.3	>220
Box3	6.02	2	0.4	>15
Box4	6.55	2	0.5	12
Box5	7.00	2	0.5	11
Box6	7.52	5	1.1	27
Box7	8.10	19	2.2	279
Box8	8.68	7	0.1	>500

Along this segment (MER and Northern part of the Eastern Rift), the geodetic moment rate is 21–99 times larger than the moment rates derived from the seismic study (Tables 3 and 4). Even if our short duration seismic data set corresponds to a random sample of the long-term pattern of seismicity over the seismic cycle, it would be unrealistic to associate such a discrepancy only with a “missing” part of the earthquake catalogue. The mean ‘missing’ $M_w = 6$ return periods are very short (6 months) in all boxes but one compared to the 39-yr-long catalogue duration and stand for at least the equivalent of 234 ‘missing’ events of a magnitude $M_w = 6$ in the catalogue for this northernmost zone (two events by year in each box and three boxes without spatial overlap).

Significant variations of the extensive style are observed in the along-axis direction of this branch showing an evolution of the second-order segmentation related to the transition between rifting of continental crust in the south to incipient oceanic floor spreading in Afar. Hayward & Ebinger (1996) studied the correlation between the morphological variations of the ~60-km-long tectono-magmatic segments within this section and in Afar (symmetrical/asymmetrical graben, the size of the graben and both the existence and the spatial distribution of the volcanic edifices within the segment) with the decrease of the crust thickness and the effective elastic thickness from south to north. Even if no clear along-axis variation in our geodetic versus seismic comparison is observed, suggesting an evolution of the extension stage, we note that the significant discrepancy between the estimates of the seismic and geodetic moment rates over the MER is similar to what is observed in the Afar area (e.g. Doubre *et al.* 2007). This implies that the aseismic behaviour of the crust reflects the control of the magma intrusion process on ~80 per cent of the total extension at short-term (e.g. Cattin *et al.* 2005; Grandin *et al.* 2009) or long-term (De Chabaliere & Avouac 1994). This is in agreement with the field observations of Casey *et al.* (2006) in the MER, and the recurrent activity of the volcanic centres (Biggs *et al.* 2011; Keir *et al.* 2011).

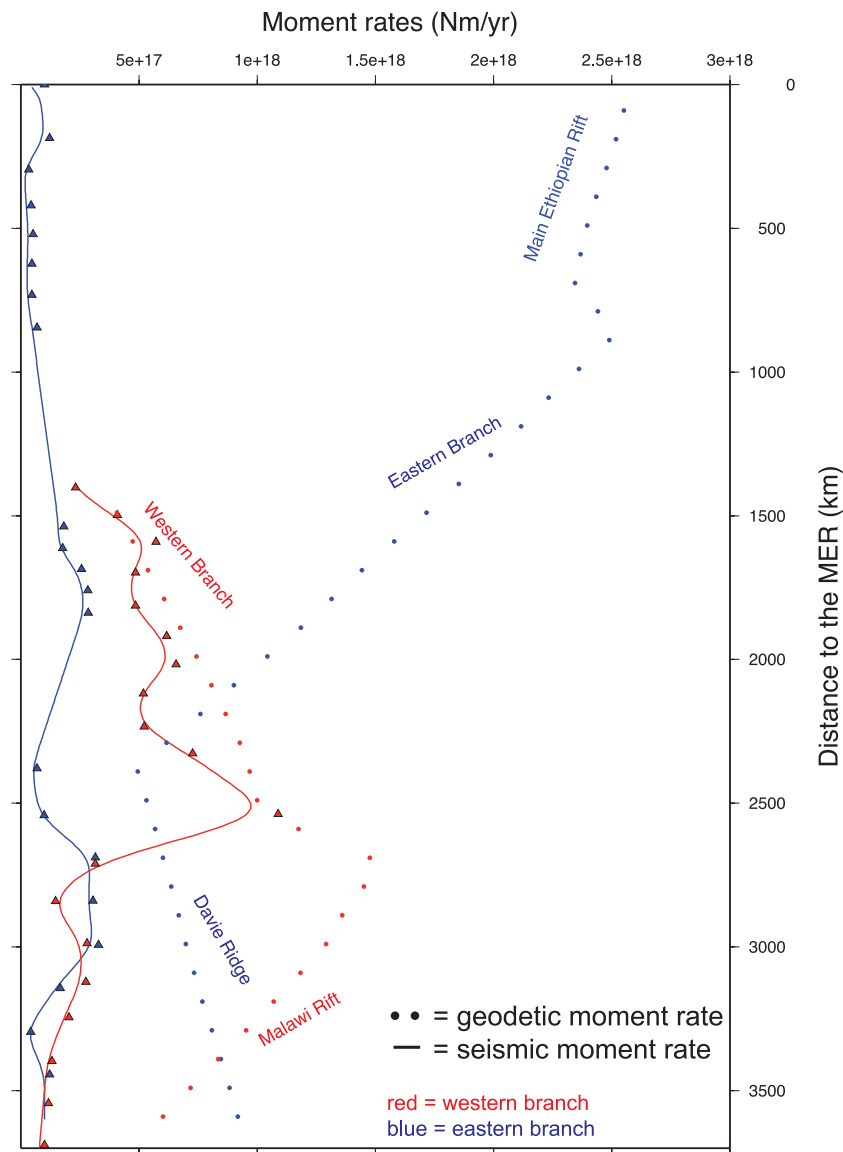


Figure 4. Seismic and geodetic moment rates along the EARS. The vertical axis corresponds to the distance along the EARS with the origin at the centre of the northernmost box. Lines = smoothed seismic moment rate (A low-pass filter is used to smooth the curve of the seismic moment rate). Triangles = seismic moment rate within each individual box. Dots = geodetic moment rate.

5.3 The southern part of the Eastern Rift (Natron rift)

We observe a decrease of the difference between seismic and geodetic moment rates in the southern tip of the Eastern branch (Fig. 7, Tables 5 and 6). However the rate of seismicity stays low, which is consistent with the associated dense distribution of volcanoes (Chorowicz 2005). Unlike MER described above, the extension accommodated by dyke intrusions was thought to be volumetrically insignificant (Ebinger *et al.* 2000). Moreover, based on structural observations and geochronology data, Ebinger *et al.* (1993) concluded that during the two main distinct volcanism episodes that occurred in this area (45–35 Ma and 18–11 Ma) the amount of extension was very low in comparison with the estimated volume of erupted material.

Nevertheless in our result, the aseismic deformation seems to be significant: the seismic moment rate reaches no more than one quarter of the geodetic moment rate at the southern end of this branch (at a latitude of about 5°S). The difference between the two estimates

stands for at least ~60 ‘missing’ earthquakes of magnitude $M_w = 6$ in the catalogue for this relatively small area (at least 1.3 event yr^{-1} within each box and two boxes without spatial overlap), which appears clearly unrealistic. Some evidences of aseismic processes have been described in previous studies, which could explain our results. For example, a recent episode of rifting in the Natron Rift observed with geodetic methods (GPS and InSAR) and a nearby temporary seismic network revealed both the importance of aseismic slip on normal fault and the role of dyke intrusion in the upper crust (Calais *et al.* 2008; Biggs *et al.* 2009; Albaric *et al.* 2010). Moreover, tomographic studies showed a wide and deep low-velocity anomaly within the upper mantle, which is evidence for a thermal anomaly currently located under the eastern margin of the Tanzanian craton (Nyblade *et al.* 2000; Nyblade 2011). All authors (Ebinger & Sleep 1998; Georges *et al.* 1998) who proposed a geodynamical model for this area argue for a great influence of a mantle plume inducing this thermal anomaly and causing a higher magmatic rate along the eastern branch than along the western one.

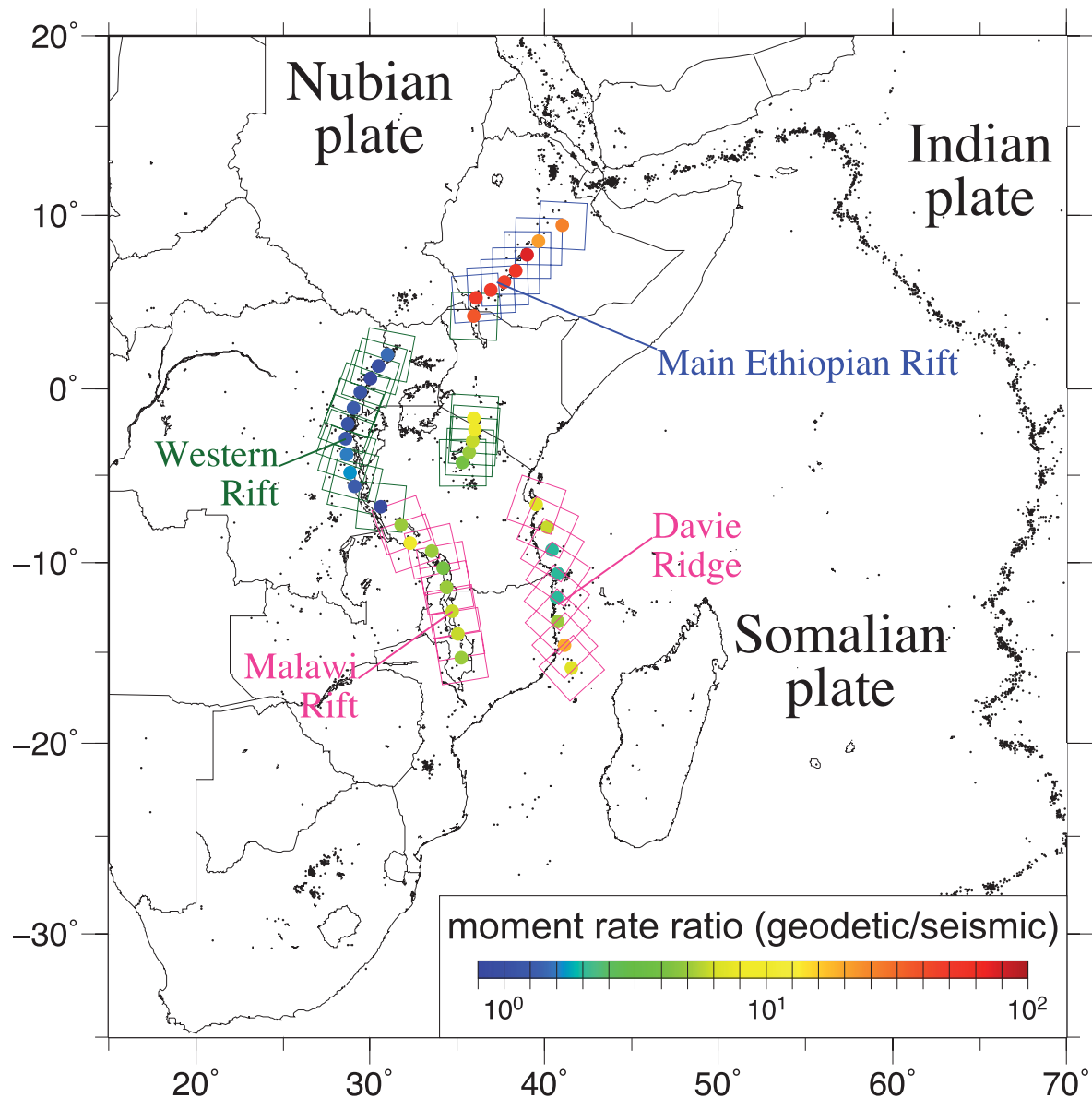


Figure 5. Ratio of the geodetic moment rate divided by the seismic moment rate, along the EARS.

5.4 The Western Rift

Along the Western branch, a significant accumulation of earthquakes with magnitude M_w between 4.5 and 5.5 together with six events with a magnitude M_w larger than 6 (M_w 6.4 in Democratic Republic of the Congo on 1992 September 11, M_w 6.2 in Uganda on 1994 February 5, M_w 6.5 on 2000 October 2, M_w 6.2 on 2002 October 24 and M_w 6.8 on 2005 December 5 in the Lake Tanganyika region) make this branch strongly seismic, particularly in comparison to the MER and the Eastern Rift (Fig. 7, Tables 7 and 8). Moreover, the location of the Nubia–Victoria pole only ~ 250 km from the northern tip of the plate boundary is responsible for the very low values of opening rates at north with a regular increase to 1.8 mm yr^{-1} at its southern tip. This leads to a similar southward increase of the moment rates, which remain on the same order of magnitude. However variations in the crustal strength had been shown in previous studies focusing on the Tanzanian Craton vicinity (Albaric *et al.* 2008), associated in particular with the recent reactivation (about 10 Ma, Kampunzu *et al.* 1998) of volcanic provinces

(Virunga, Kivu provinces); the low rate of melt production together with the magma composition (Rogers *et al.* 1998) recorded in these provinces are characteristic of an early continental extension stage. The amount of the extension is also not large enough to promote a significant ductile stretching and a potentially aseismic deformation (Bastow & Keir 2011). This is also consistent with the remoteness of the mantle plume assumed to underlie the Eastern Rift (see previous paragraph) (Rogers *et al.* 1998).

5.5 The Malawi Rift

The Mbeya area connects the South Rukwa and North Malawi Rifts (Fig. 8, Tables 9 and 10). It is also the triple junction between the Nubia, Victoria and Rovuma plates. In term of tectonics, this zone is complex with some compression ‘pulses’ within a global environment of normal faulting (Delvaux & Barth 2010). The seismic moment rate computed using the scalar approach does not take into account this complexity. The Malawi Rift is thought to be a good

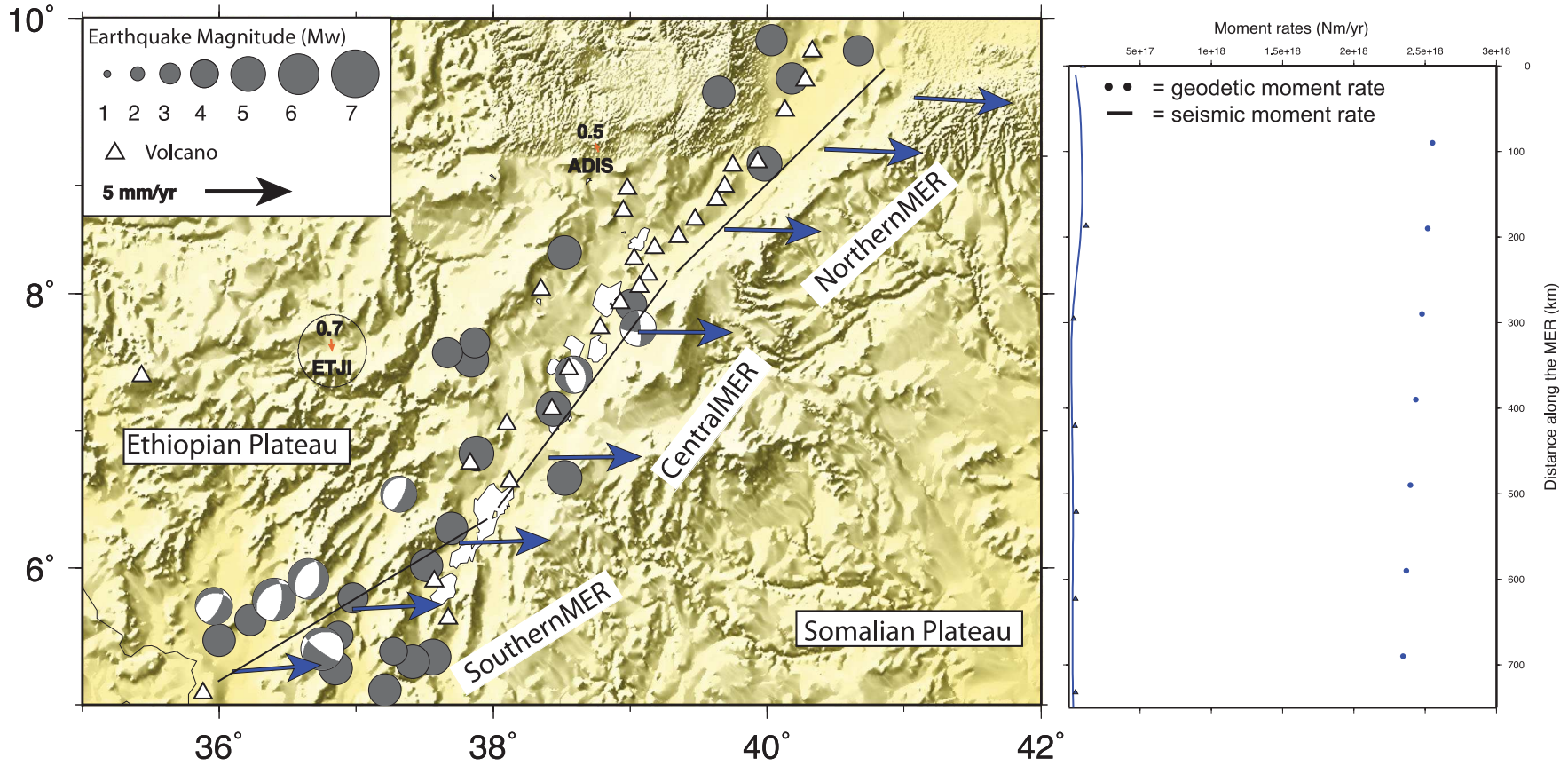


Figure 6. Zoom on the Main Ethiopian Rift. The blue arrows correspond to the velocity model at the frontier between Nubia and Somalia plates in the Nubian reference frame. The orange arrows correspond to the GPS velocity w.r.t. Nubia. The grey circles depict the seismicity and we add the known focal mechanisms (source NEIC and ISC catalogues). The white triangles represent the volcanoes with recent activity (source NGDC).

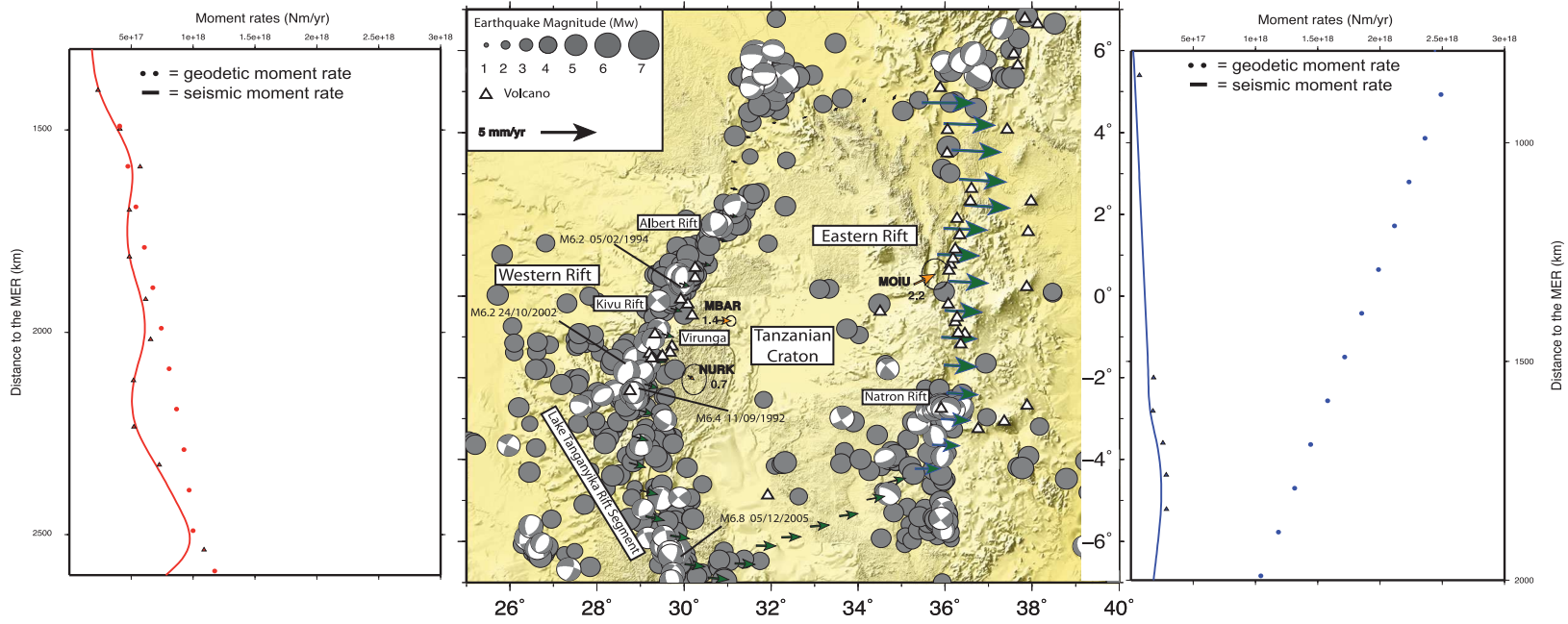


Figure 7. Zoom on the Victoria Plate. The green arrows correspond to the velocity model at the frontier between Nubia and Victoria (along the Western rift) w.r.t. Nubia and between Somalia and Victoria plates (along the Eastern rift) with a fixed Victoria reference frame. Orange arrows, grey circles, white triangles: same as Fig. 6.

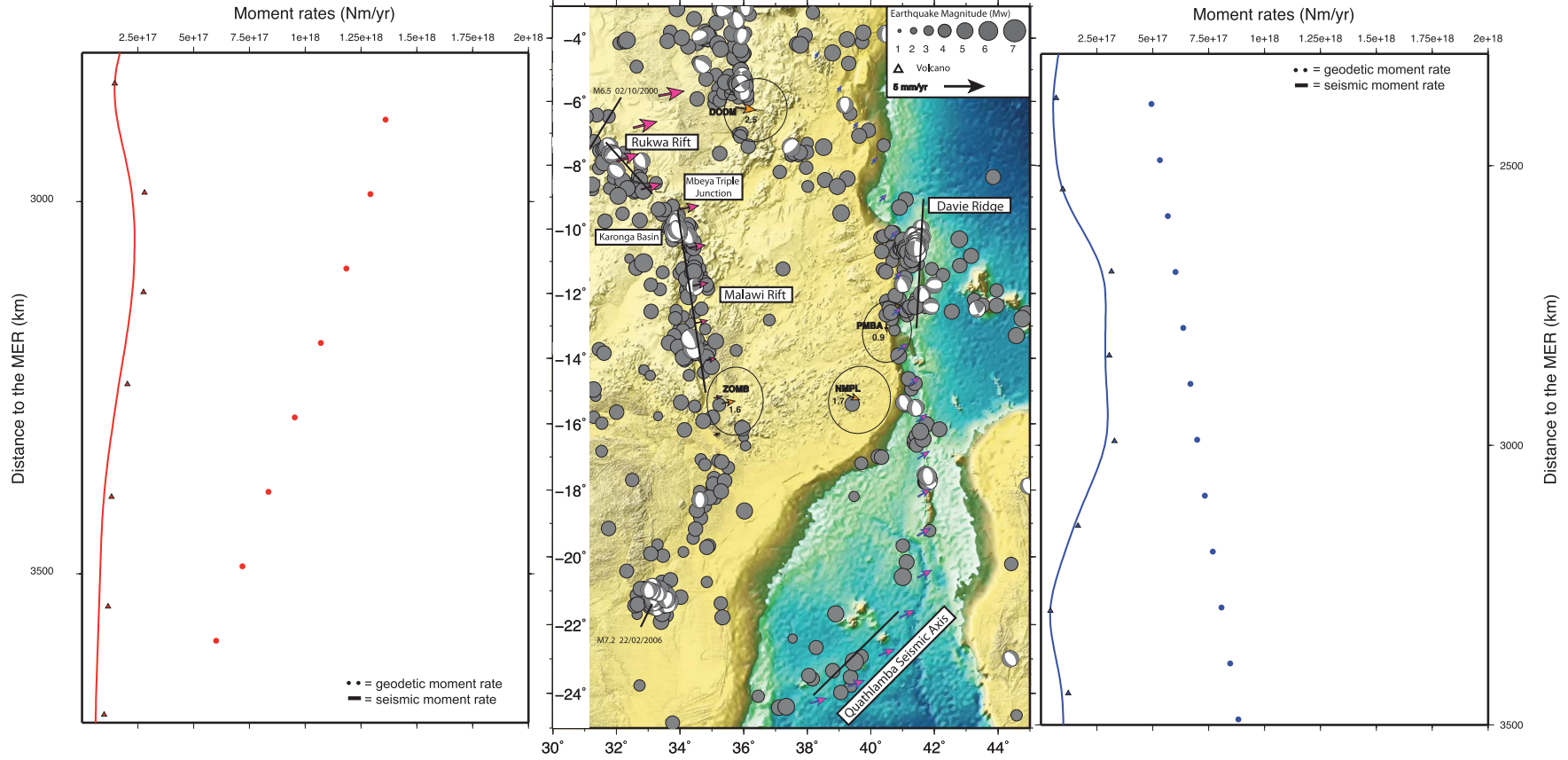


Figure 8. Zoom on the Rovuma Plate. The pink arrows correspond to the velocity model at the frontier between Nubia and Rovuma (along the Rukwa and Malawi rifts) w.r.t. Nubia; and between Somalia and Rovuma plates (along the Davie Ridge and the Quathlamba Seismic Axis) with fixed Rovuma. Orange arrows, grey circles, white triangles: same as Fig. 6.

example of initial rift stage (Chorowicz 2005), without fluid involvement or aseismic slip (Biggs *et al.* 2010). Our results show a seismic moment rate four to nine times smaller than the geodetic moment rate, but some field observations denoted geological structures (see in particular the description of the Bilila-Mtakataka fault by Jackson & Blenkinsop 1997), which present the necessary conditions to trigger a normal faulting earthquake with magnitude as large as $M_w = 8$ and so a return period clearly larger than the catalogue used here. So it is reasonable to assume a 'missing' event of such a magnitude, which would greatly modify the shape of the seismic moment rate curve upward to reach values of the same range than the geodetic one.

5.6 The Davie Ridge

From the study of the focal mechanisms, Delvaux & Barth (2010) deduce that an E–W extension occurs along the Davie Ridge. This ridge is considered to be the southward continuation of the eastern branch of the EARS. This structure, which was originally a transform structure, is associated with a significant level of scattered seismicity (Grimison & Chen 1988). Moreover, this branch partly under water and less studied than the segments described above, might encompass an also significant number of likely missing events. This could reasonably explain the seismic moment rates more than two times lower than the geodetic one in five over eight boxes along the Davie Ridge.

We can notice a better agreement of the seismic moment rate with the geodetic one at the segment center, pattern similar to the one observed along the Malawi Rift (Fig. 8, Tables 11 and 12). This quasi-symmetrical evolution observed in the two moment rate relative values between the two sides of the Rovuma Plate, leads us to follow the assumption of a diffuse extension zone through Mozambique (Grimison & Chen 1988; Kusky *et al.* 2010).

6 CONCLUSION

Using the largest data set from permanent African GPS networks currently available, we bring out a large-scale model of the kinematics in Africa, particularly focusing on the EARS system. We accurately determined the Euler pole of the Nubia Plate with respect to ITRF-2008, which is consistent with the results from Altamimi *et al.* (2012). Similar to Calais *et al.* (2006) and Stamps *et al.* (2008), the velocity field in Eastern Africa requires the taking into account of two micro plates (Victoria and Rovuma) delimited by the active branches of the EARS. However, the Euler poles of the Somalia Plate and of the two micro plates (Victoria and Rovuma) remains insufficiently constrained due to either a lack of GPS sites in these area (largely under sea for the Somalia Plate and difficult to access) or to recent installations of GPS stations that impede reliable velocity values, particularly for the Rovuma Plate where most of the stations are younger than 2 yr. In spite of these restrictions, we designed a geodetic model which fits the data and which is consistent with both previous geodetic studies and tectonic observations. We observed in this study that, even if an improvement may be expected after a few years (increase of the time-series length, densification of the GPS network), we already obtain a model in a good adequacy with the data set collected here.

Using all the available data from the earthquake catalogues (NEIC, ISC) from the 1973 to 2012, we compare our geodetic results to the seismic activity along the whole EARS. The main

limitation encountered here is related to the completeness of the seismic catalogues: the potential microseismicity not taken into account and above all the lack in the recorded seismicity of large events (too old or coming) due to the time length of the seismic cycle. Using a simple scalar approach, this study focuses on the spatial evolution of the rifting process along the EARS by looking at the seismic versus geodetic moment rates along the four main branches of the EARS.

By analysing the required 'missing' part of the catalogue to equal seismic and geodetic results, keeping in mind the tectonic environment of each area (and by inference the largest magnitude reasonably expected), our results allow us to differentiate the zones where aseismic deformation (associated with a weaker lithosphere, Bastow & Keir 2011) seems to significantly account for the middle-term extension from the more seismic ones.

The EARS offers all ranges of rift morphologies: from the Main Ethiopian Rift, where segments present the characteristics of the last stage before seafloor spreading with an extension mainly by dyke intrusions, to the nascent signs of continental extension in Mozambique, where large normal active faults play the main role in the extension. An accurate description of the relations between the tectonic characteristics, thermal structure and kinematics is beyond the scope of this study (for more details refer to the works of Ebinger *et al.* 2012).

However we clearly see a global increase of the accommodation of the deformation by seismic activity from north to south. This seems to reflect the evolution of the extension style. In the north, the influence of the Afar hotspot decreases the elastic thickness of the lithosphere, and local volcanism participates in the extension process of the lithosphere (dyking) with a relatively small release of seismic energy. In the south, the tectonic structures have typical features of the early rifting stages with earthquakes triggered by the deformation of the cold, brittle crust. These observations testify to the parallel evolution of the thermal state of the lithosphere and its surface expression (Ebinger *et al.* 1993; Bonini *et al.* 2005; Kurz *et al.* 2007; Yang & Chen 2008; Raucoules *et al.* 2010).

The large discrepancy between geodetic and seismic moment rates is largely related to the existence of volcanic activity as shown along the MER or the Eastern rift. Conversely a good agreement is found within the zones where the rift is not affected by volcanism and the lithospheric strength is high. Therefore the main parameter to influence the discrepancy between seismic and geodetic results appears to be the proportion of ductile deformation (and by inference the lithospheric thermal state). And even if the presence of magmatism and/or volcanism is commonly the signature of the extension processes for a mature rift, whose the weaker lithosphere is related to a high degree of thinning caused by a previous extension over a long time (Bastow & Keir 2011); other causes of lithospheric weakening can be found (mantle plume for example) triggering also a decrease of the amount of extension by faulting (and by inference a decreasing seismic rate).

This spatial evolution of the geodetic/seismic moment ratio for continental to more mature domain is also pointed out by Nobile *et al.* (2012) for short-term deformation involving dyke intrusion. Whereas the dyking events along the Manda-Harraro segment and Dallol area in Afar monitored by both InSAR and seismic network over the last decade (Wright *et al.* 2006; Ayele *et al.* 2007, 2009; Grandin *et al.* 2009, 2011; Wright *et al.* 2012) are characterized by very high geodetic/seismic ratio (higher than 25), the intrusions of Natron at the Southern end of the Eastern Rift (Calais *et al.* 2008), and the Harrat Lunayyir (Pallister *et al.* 2010) within the Arabian Plate show lower ones (lower than 10).

ACKNOWLEDGEMENTS

We would like to thank all the people involved in the installation and the maintenance of the GPS stations and make data available. This paper was supported by the French Agence Nationale pour la Recherche (DoRA project, ANR-09-JCJC-0051-01). We thank the Editor, Dr. Saskia Goes and the two anonymous reviewers for their thoughtful reviews and comments.

The maps in this paper were produced using the public domain Generic Mapping Tools (GMT) software (Wessel & Smith 1995).

REFERENCES

- Albaric, J., Déverchère, J., Petit, C., Perrot, J. & LeGall, B., 2008. Crustal rheology and depth distribution of earthquakes: insights from the central and southern East African Rift System, *Tectonophysics*, **468**, 28–41.
- Albaric, J. *et al.*, 2010. Contrasted seismogenic and rheological behaviours from shallow and deep earthquake sequences in the North Tanzanian Divergence, East Africa, *J. Afric. Earth Sci.*, **58**, 799–811.
- Altamimi, Z., Métivier, L. & Collilieux, X., 2012. ITRF2008 plate motion model, *J. geophys. Res.*, **117**, B07402, doi:10.1029/2011JB008930.
- Asfaw, L.M., 1998. Environmental hazard from fissures in the Main Ethiopian Rift, *J. Afric. Earth Sci.*, **27**(3/4), 481–490.
- Ayele, A. *et al.*, 2007. The volcano seismic crisis in Afar, Ethiopia, starting September 2005, *Earth planet. Sci. Lett.*, **255**, 177–187.
- Ayele, A. *et al.*, 2009. The September 2005 mega-dike emplacement in the Manda-Harraro nascent oceanic rift (Afar depression), *Geophys. Res. Lett.*, **36**, L20306, doi:10.1029/2009GL039605.
- Bastow, I.D. & Keir, D., 2011. Protracted development of a magmatic rifted margin in Afar, *Nat. Geosci.*, **4**, 248–250.
- Bendick, R., McClusky, S., Bilham, R., Asfaw, L. & Klemperer, S., 2006. Distributed Nubia Somalia relative motion and dike intrusion in the Main Ethiopian Rift, *Geophys. J. Int.*, **165**, 303–310.
- Biggs, J., Amelung, F., Gourmelen, N., Dixon, T.H. & Kim, S., 2009. InSAR observations of 2007 Tanzania rifting episode reveal mixed fault and dyke extension in an immature continental rift, *Geophys. J. Int.*, **179**, 549–558.
- Biggs, J., Nissen, E., Craig, T., Jackson, J. & Robinson, D.P., 2010. Breaking up the hanging wall of a rift-border fault: the 2009 Karonga earthquakes, Malawi, *Geophys. Res. Lett.*, **37**, 11305, doi:10.1029/2010GL043179.
- Biggs, J., Bastow, I.D., Keir, D. & Lewi, E., 2011. Pulses of deformation reveal frequently recurring shallow magmatic activity beneath the Main Ethiopian Rift, *Geochem., Geophys., Geosyst.*, **12**, Q0AB10, doi:10.1029/2011GC003662.
- Bilham, R., Bendick, R., Larson, K., Braun, J., Tesfaye, S., Mohr, P. & Asfaw, L., 1999. Secular and tidal strain across the Ethiopian rift, *Geophys. Res. Lett.*, **27**, 2789–2984.
- Bonini, M., Corti, G., Innocenti, F., Manetti, P., Mazzarini, F., Abebe, T. & Pecskey, Z., 2005. Evolution of the Main Ethiopian Rift in the frame of Afar and Kenya rifts propagation, *Tectonics*, **24**, TC1007, doi:10.1029/2004TC001680.
- Calais, E., Ebinger, C., Hartnady, C. & Nocquet, J.M., 2006. Kinematics of the East African Rift from GPS and earthquake vector data, in *The Afar Volcanic Province within the East African Rift System*, Vol. 259, pp. 9–22, eds Yirgu, G., Ebinger, C.J. & Maguire, P.K.H., Geological Society London Special Publications.
- Calais, E. *et al.*, 2008. Strain accommodation by slow slip and dyking in a youthful continental rift, East Africa, *Nature*, **456**, 783–787.
- Casey, M., Ebinger, C., Keir, D., Gloaguen, R. & Mohamed, F., 2006. Strain accumulation in transitional rifts: extension by magma intrusion and faulting in Ethiopian rift magmatic segments, in *The Afar Volcanic Province within the East African Rift System*, Vol. 259, pp. 143–163, eds Yirgu, G., Ebinger, C.J. & Maguire, P.K.H., Geological Society London Special Publications.
- Cattin, R., Doubre, C., De Chabalier, J.-B., Vigny, C., King, G., Avouac, J.-P. & Ruegg, J.-C., 2005. Numerical modelling of Quaternary deformation and post-rifting displacement in the Asal-Ghoubbet Rift (Djibouti, Aar), *Earth planet. Sci. Lett.*, **239**, 352–367.
- Chorowicz, J., 2005. The East African Rift System, *J. Afric. Earth Sci.*, **43**, 79–410.
- D'Agostino, N. *et al.*, 2009. Contemporary crustal extension in the Umbria-Marche Apennines from regional CGPS networks and comparison between geodetic and seismic deformation, *Tectonophysics*, **476**, 3–12.
- De Chabalier, J.B. & Avouac, J.P., 1994. Kinematics of the Asal Rift (Djibouti) determined from the deformation of Fieale Volcano, *Science*, **265**, 1677–1681.
- Delvaux, D. & Khan, A., 1998. Tectonics, sedimentation and volcanism in the East African Rift System: introduction, *J. Afric. Earth Sci.*, **26**(3), 343–346.
- Delvaux, D. & Barth, A., 2010. African Stress Pattern from formal inversion of focal mechanism data. Implications for rifting dynamics, *Tectonophysics*, **482**, 105–128.
- Doubre, C., Manighetti, I., Dorbath, L., Dorbath, C., Bertil, D. & Delmond, J.C., 2007. Crustal structure and magmato-tectonic processes in an active rift (Asal-Ghoubbet, Afar, East-Africa). Part 2: insights from the 23 years recording of seismicity since the last rifting event, *J. geophys. Res.*, **112**(B5), 5406, doi:10.1029/2006JB004333.
- Ebinger, C.J., 1989a. Geometric and kinematic development of border faults and accommodation zones, Kivu–Rusizi Rift, Africa, *Tectonics*, **8**(1), 117–133.
- Ebinger, C., 1989b. Tectonic development of the western branch of the East African rift system, *Geol. Soc. Am. Bull.*, **101**, 885–903.
- Ebinger, C.J., Bechtel, T.D., Forsyth, D.W. & Bowin, C.O., 1989. Effective elastic plate thickness beneath the East African and Afar Plateaus and dynamic compensation of the uplifts, *J. geophys. Res.*, **94**(B3), 2883–2901.
- Ebinger, C. & Casey, M., 2001. Continental breakup in magmatic provinces: an Ethiopian example, *Geology*, **29**, 525–530.
- Ebinger, C. & Sleep, N., 1998. Cenozoic magmatism throughout East Africa resulting from impact of a single plume, *Nature*, **395**, 788–791.
- Ebinger, C., Yemane, T., WoldeGabriel, G., Aronson, J. & Walter, R., 1993. Eocene-recent volcanism and faulting in the southern Main Ethiopian rift, *Geol. Soc. Lond.*, **150**, 99–108.
- Ebinger, C., Yemane, T., Harding, D.J., Tesfaye, S., Kelley, S. & Rex, D.C., 2000. Rift deflection, migration, and propagation: linkage of the Ethiopian and Eastern Rifts, Africa, *Geol. Soc. Am. Bull.*, **112**, 163–176.
- Ebinger, C., Lindsey, J., Ayele, A. & Belachew, M., 2012. Seismic and geodetic evaluation of earthquake and volcanic hazards in East Africa, in *Proceedings of the Magmatic Rifting and Active Volcanism Conference*, Addis Ababa, January 2012.
- Fernandes, R.M.S., Ambrosius, B.A.C., Noomen, R., Bastus, L., Combrinck, L., Miranda, J.M. & Sapkman, W., 2004. Angular velocity of Nubia and Somalia from continuous GPS data: implications on present-day relative kinematics, *Earth planet. Sci. Lett.*, **222**, 197–208.
- George, R., Rogers, N. & Kelley, S., 1998. Earliest magmatism in Ethiopia: evidence for two mantle plumes in one flood basalt province, *Geology*, **26**, 923–926.
- Grandin, R. *et al.*, 2009. September 2005 Manda Hararo Dabbahu rifting event, Afar (Ethiopia): constraints provided by geodetic data, *J. geophys. Res.*, **114**, B08404, doi:10.1029/2008JB005843.
- Grandin, R. *et al.*, 2011. Seismicity during lateral dike propagation: Insights from new data in the recent Manda Hararo–Dabbahu rifting episode (Afar, Ethiopia), *Geochem., Geophys., Geosyst.*, **12**, Q0AB08, doi:10.1029/2010GC003434.
- Grimison, N.L. & Chen, W.P., 1988. Earthquakes in Davie Ridge–Madagascar region and the southern Nubian–Somalian plate boundary, *J. geophys. Res.*, **93**(B9), 10 439–10 450.
- Hartnady, C.J.H., 2002. Earthquake hazard in Africa: perspectives on the Nubia-Somalia boundary, *S. Afric. J. Sci.*, **98**, 425–428.
- Hayward, N.J. & Ebinger, C.J., 1996. Variations in the long-axis segmentation of the Afar Rift system, *Tectonics*, **15**(2), 244–257.
- Hyndman, R.D. & Weichert, D.H., 1983. Seismicity and rates of relative plate motion on the plate boundaries of western North America, *Geophys. J. R. astr. Soc.*, **72**, 59–82.

- Jackson, J. & Blenkinsop, T., 1997. The Bilila-Mtakataka Fault in Malawi; an active, 100-km long, normal fault segment in thick seismogenic crust, *Tectonics*, **16**, 137–150.
- Jenny, S., Goes, S., Giardini, D. & Kahle, H.G., 2004. Earthquake recurrence parameters from seismic and geodetic strain rates in eastern Mediterranean, *Geophys. J. Int.*, **157**, 1331–1347.
- Jestin, F., Huchon, P. & Gaulier, J.M., 1994. The Somalia plate and East African rift system: present-day kinematics, *Geophys. J. Int.*, **116**, 637–654.
- Joffe, F. & Garfunkel, Z., 1987. Plate kinematics of the circum Red Sea—a reevaluation, *Tectonophysics*, **141**, 5–22.
- Kamunzu, A.B., Bonhomme, M.G. & Kanika, M., 1998. Geochronology of volcanic rocks and evolution of the Cenozoic Western Branch of the East African rift system, *J. Afric. Earth Sci.*, **26**(3), 441–461.
- Kanamori, H., 1977. The energy release in great earthquakes, *J. geophys. Res.*, **82**, 1981–1987.
- Keir, D., Stuart, G.W., Jackson, A. & Ayele, A., 2006. Local earthquake magnitude scale and seismicity rate for the Ethiopian Rift, *Bull. seism. Soc. Am.*, **96**(6), 2221–2230.
- Keir, D., Pagli, C., Bastow, I.D. & Ayele, A., 2011. The magma-assisted removal of Arabia in Afar: evidence from dike injection in the Ethiopian rift captured using InSAR and seismicity, *Tectonics*, **30**, TC2008, doi:10.1029/2010TC002785.
- King, R.W. & Bock, Y., 2010. *Documentation for the GAMIT/GLOBK GPS software analysis, release 10.04*, Massachusetts Institute of Technology, Cambridge.
- Kogan, L., Fisseha, S., Bendick, R., Reilinger, R., McClusky, S., King, R. & Solomon, T., 2012. Lithospheric strength and strain localization in continental extension from observations of the East African Rift, *J. geophys. Res.*, **117**, B03402, doi:10.1029/2011JB008516.
- Kostrov, B., 1974. Seismic moment and energy of earthquakes and seismic flow of rock, *Izvestiya, Academy of Sciences, USSR Phys. Solid Earth*, **1**, 23–40.
- Kreemer, C., Holt, W.E., Goes, S. & Govers, R., 2000. Active deformation in eastern Indonesia and the Philippines from GPS and seismicity data, *J. geophys. Res.*, **105**, 663–680.
- Kreemer, C., Holt, W.E. & Haines, A.J., 2002. The global moment rate distribution within plate boundary zones, in *Plate Boundary Zones, AGU Geodynamics Series 30*, pp 173–190, eds Stein, S. & Freymueller, J.T., American Geophysical Union, Washington, DC.
- Kurz, T., Gloaguen, R., Ebinger, C., Casey, M. & Abebe, B., 2007. Deformation distribution and type in the Main Ethiopian Rift (MER); a remote sensing study, *J. Afric. Earth Sci.*, **48**(2–3), 100–114.
- Kusky, T.M., Toraman, E., Raharimahefa, T. & Rasoazanamparany, C., 2010. Active tectonics of the Alaotra-Ankay graben system, Madagascar: possible extension of Somalian-African Diffusive Plate Boundary? *Gondwana Res.*, **18**(2–3), 274–294.
- Le Gall, B. *et al.*, 2004. Neogene-Recent rift propagation in central Tanzania: morphostructural and aeromagnetic evidence from the Kilombero area, *Geol. Soc. Am. Bull.*, **116**, 490–510.
- Mao, A., Harrison, C.G.A. & Dixon, T.H., 1999. Noise in GPS coordinate time series, *J. geophys. Res.*, **104**, 2797–2816.
- Masson, F., Chery, J., Hatzfeld, D., Martinod, J., Vernant, P., Tavakoli, F. & Ghafory-Ashstiani, M., 2005. Seismic versus aseismic deformation in Iran inferred from earthquakes and geodetic data, *Geophys. J. Int.*, **160**, 217–226.
- Mazzotti, S., Leonard, L.J., Cassidy, J.F., Rogers, G.C. & Halchuk, S., 2011. Seismic hazard in western Canada from GPS strain rates versus earthquake catalog, *J. geophys. Res.*, **116**, B12310, doi:10.1029/2011JB008213.
- Nobile, A., Pagli, C., Keir, D., Wright, T.J., Ayele, A., Ruch, J. & Acocella, V., 2012. Dike-fault interaction during the 2004 Dallol intrusion at the northern edge of the Erta Ale Ridge (Afar, Ethiopia), *Geophys. Res. Lett.*, **39**, L19305, doi:10.1029/2012GL053152.
- Nocquet, J.-M., 2002. *Mesure de la déformation crustale en Europe occidentale par géodésie spatiale, Thèse de doctorat*, Université de Nice-Sophia-Antipolis.
- Nocquet, J.M., Willis, P. & Garcia, S., 2006. Plate kinematics of Nubia-Somalia using a combined DORIS and GPS solution, *J. Geod.*, **80**, 591–607.
- Nyblade, A., 2011. The upper mantle low velocity anomaly beneath Ethiopia, Kenya and Tanzania: constraints on the origin of the African superswell in eastern Africa and plate versus plume models of mantle dynamics, Volcanism and Evolution of the African Lithosphere, *Geol. Soc. Am. Spec. Papers*, **478**, 37–50.
- Nyblade, A., Owens, T., Gurrrola, H., Ritsema, J. & Langston, C., 2000. Seismic evidence for a deep upper mantle thermal anomaly beneath east Africa, *Geology*, **28**, 599–602.
- Pallister, J.S., McCauslan, W.A. & Jonsson, S., 2010. Broad accommodation of rift-related extension recorded by dyke intrusion in Saudi Arabia, *Nat. Geosci.*, **3**, 705–712.
- Pancha, A., Anderson, J.G. & Kreemer, C., 2006. Comparison of seismic and geodetic scalar moment rates across the basin and range province, *Bull. seism. Soc. Am.*, **96**, 11–32.
- Papazachos, C. & Kiratzi, A., 1992. A formulation for reliable estimation of active crustal deformation and its application to central Greece, *Geophys. J. Int.*, **111**, 424–432.
- Raucoules, D., Ristori, B., de Michele, M. & Briole, P., 2010. Surface displacement of the M(w) 7 Machaze earthquake (Mozambique): complementary use of multiband InSAR and radar amplitude image correlation with elastic modelling, *Remote Sens. Environ.*, **114**(10), 2211–2218.
- Rezapour, M., 2005. Magnitude scale in the Tabriz seismic network, *J. Earth Space Phys.*, **31**(1), 13–21.
- Rogers, N.W., James, D., Kelley, S.P. & DeMulder, M., 1998. The generation of potassic lavas from the eastern Virunga province, Rwanda, *J. Petrol.*, **39**, 1223–1247.
- Scordilis, E.M., 2006. Empirical global relations converting Ms and mb to moment magnitude, *J. Seismol.*, **10**, 225–236.
- Shen-Tu, B., Holt, W.E. & Haines, A.J., 1998. Contemporary kinematics of the Western United States determined from earthquake moment tensors, very long baseline interferometry, and GPS observations, *J. geophys. Res.*, **103**, 18 087–18 117.
- Stamps, D.S., Calais, E., Saria, E., Hartnady, C., Nocquet, J.M., Ebinger, C. & Fernandez, R.M., 2008. A kinematic model for the East African Rift, *Geophys. Res. Lett.*, **35**, L05304, doi:10.1029/2007GL032781.
- Ward, S.N., 1998. On the consistency of earthquake moment rates, geological fault data, and space geodetic strain: the United States, *Geophys. J. Int.*, **134**, 172–186.
- Weichert, D.H., 1980. Estimation of the earthquake recurrence parameters from unequal observation periods for different magnitudes, *Bull. seism. Soc. Am.*, **70**, 1337–1346.
- Wessel, P. & Smith, W.H.F., 1995. New version of the generic mapping tools released, *EOS, Trans. Am. geophys. Un.*, **76**, 329.
- Williams, S.D.P., 2003. The effect of coloured noise on the uncertainties of rates estimated from geodetic time series, *J. Geod.*, **76**, 483–494.
- Williams, S.D.P., 2008. CATS: GPS coordinate time series analysis software, *GPS Solut.*, **12**, 147–153.
- Wright, T.J., Ebinger, C., Biggs, J., Ayele, A., Gezahegn, Y., Yirgu, D., Keir, D. & Stork, A., 2006. Magma-maintained rift segmentation at continental rupture in the 2005 Afar dyking episode, *Nature*, **442**, 291–294.
- Wright, T. *et al.*, 2012. Geophysical constraints on the dynamics of spreading centres from rifting episodes on land, *Nat. Geosci.*, **5**, 242–249.
- Yang, Z. & Chen, W.-P., 2008. Mozambique earthquake sequence of 2006: high-angle normal faulting in southern Africa, *J. geophys. Res.*, **113**, B12303, doi:10.1029/2007JB005419.
- Yang, Z.-H. & Chen, W.-P., 2010. Earthquakes along the East African Rift System: a system-wide, multi-scale perspective, *J. geophys. Res.*, **115**, B12309, doi:10.1029/2009JB006779.
- Zhang, J., Bock, Y., Johnson, H., Fang, P., Williams, S., Genrich, J., Wdowinski, S. & Behr, J., 1997. Southern California permanent GPS geodetic array: error analysis of daily position estimates and sites velocities, *J. geophys. Res.*, **102**, 18 035–18 055.